Indian Journal of Pure & Applied Physics
Vol. 64, April 2026, pp. 409-417
DOI: 10.56042/ijpap.v64i4.27155

Quantum Simulation of One-Dimensional Crystal Band Structure with a Tunable Superconducting Electric Circuit

N G Berezkin*

Landau Phystech School of Physics and Research, Moscow Institute of Physics and Technology National Research University, Dolgoprudny 141701, Moscow Region, Russia

Received: 3rd January 2026; accepted: 19th February 2026

This paper presents a concept for a quantum simulator based on a superconducting qubit coupled to a readout resonator, designed to experimentally emulate the band structure of a one-dimensional crystal. The superconducting qubit, with its intrinsic periodic potential from the Josephson effect, serves as a direct analog of an electron in a periodic lattice. The Hamiltonian of the system is analyzed in two complementary regimes: the weak-coupling regime, corresponding to nearly-free electrons, and the strong-coupling regime, corresponding to electrons in the tight-binding limit. We show that the system can be continuously swept between these regimes using a flux-tunable symmetric DC-SQUID to vary the effective Josephson energy. To probe the resulting band structure, we propose an experimental method based on two-tone spectroscopy, which maps the qubit's flux-dependent transition spectrum via the dispersive shift of a coupled resonator. Numerical simulations confirm the feasibility of this approach, visualizing the transition from a broad band dispersion in the weak-coupling limit to exponentially narrow bands in the strong-coupling limit. This platform demonstrates how tunable superconducting circuits can be used as versatile quantum simulators for fundamental solid-state physics phenomena.

Keywords: Quantum simulation, Josephson effect, Superconducting qubit, SQUID, Two-tone spectroscopy

1 Introduction

Currently, small-scale superconducting circuit-based systems are primarily used in the field of verifying fundamental principles of quantum computing and demonstrating proof-of-concept for various architectures[1-3]. There exists an alternative paradigm for utilizing such platforms: it involves the direct use of the native quantum properties of these artificially created systems for the experimental study of fundamental physical models. High parameter controllability, configurable interactions, and advanced state readout techniques enable the implementation of Hamiltonians describing collective effects and phase transitions in model quantum systems. Previous studies on quantum simulators have employed various approaches that exploit quantum phenomena in qubit arrays. For instance, the suitability of fixed-frequency transmon qubits with fixed interactions for the analogue quantum simulation of spin systems has been assessed[4]. Separately, a transmon chain realizing the Bose–Hubbard model with attractive interactions was presented[5]. The qubits in this chain incorporate asymmetric SQUIDs, enabling the degree of disorder in the system to be tuned via a uniform external magnetic field. This idea is generalized in further work[6] to the case of a two-dimensional transmon array. This work presents a fundamentally different concept of a quantum simulator based on a single qubit coupled to a readout resonator, demonstrating that the system reproduces the band structure of a model one-dimensional crystal. To tune the energy levels of the artificial quantum system under consideration, we propose employing a symmetric SQUID, whose Josephson energy turns to zero at a specific value of the applied magnetic flux.

The central part of the proposed device is a superconducting qubit. It is a circuit whose quantum behavior originates from the Josephson effect — the coherent tunneling of Cooper pairs through a thin insulating barrier[7]. This effect provides a periodic potential $U(\varphi) = -E_J \cos\varphi$ for the superconducting phase difference φ, making the superconducting qubit an artificial analog of an electron in a one-dimensional crystal lattice. The qubit Hamiltonian is

$$\hat{H} = 4E_C\left(\hat{n} - n_g\right)^2 - E_J \cos\hat{\varphi} \qquad \dots (1)$$

where $\hat{\varphi}$ is the phase operator and $\hat{n}$ is the Cooper-pair number operator, satisfying the commutation

---

*Corresponding author: E-mail: berezkin.ng@phystech.edu relation $[\hat{\varphi}, \hat{n}] = i$. Effective circuit diagram of the superconducting qubit is shown in Fig. 1. The Josephson junction provides a periodic potential $U(\varphi) = -E_J \cos\varphi$, while the gate charge $n_g = C_g V_g/(2e)$ is controlled by an external voltage V_g.

A direct analogy exists between this Hamiltonian and that of an electron in a one-dimensional periodic crystal: $\hat{\varphi}$ plays the role of a spatial coordinate, and $\hat{n}$ corresponds to the quasimomentum. The first term in the Hamiltonian (1) represents kinetic energy, and the second a cosine lattice potential. As in a solid, band gaps open at the Brillouin zone boundaries due to Bragg scattering, which forbids propagating waves with wavevectors at the zone edge. At these points the eigenstates become standing waves, symmetric or antisymmetric with respect to the potential minima, leading to an energy splitting. The existence of such band gaps has a simple qualitative interpretation: solutions to the Schrödinger equation at the Brillouin zone boundary can only have the form of standing waves. Referring to the Josephson junction potential shown in Fig. 2, since the interaction potential of a particle with such a chain of "atoms" is symmetric with respect to zero, the probability distribution of finding a particle at a given location must also be symmetric with respect to zero. Consequently, standing wave solutions with the Brillouin wave vector can be either even or odd. In one case, the probability density has maxima at the "atomic" sites, while in the other, it has minima at the "atomic" positions. For a free particle, these states would have the same energy; however, in the periodic potential, due to such spatial probability distribution, the energies of these states are different. The qubit spectrum therefore naturally exhibits a one-dimensional crystal band structure.

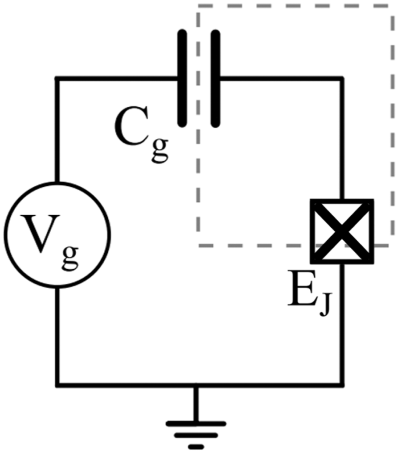

Fig. 1 — Effective circuit diagram of the superconducting qubit: Josephson junction shunted by the capacitance

2 Methods

The stationary Schrödinger equation for Hamiltonian (1) can be solved exactly in the phase basis using special Mathieu functions[8]. However, this paper does not employ this analytical solution but instead take a different approach, inspired by the physical analogy. In the following sections we analyze Hamiltonian (1) in two complementary limits: the weak-coupling regime ($E_J \lesssim E_C$), corresponding to a shallow potential and nearly-free electrons, and the strong-coupling regime ($E_J \gg E_C$), corresponding to deep wells and tightly bound electrons. The method of sweeping the quantum simulator between these regimes and the experimental concept are then presented.

2.1 Weak-Coupling Regime

When E_J is relatively small ($E_J \lesssim E_C$), the periodic potential $U(\varphi) = -E_J \cos\varphi$ can be treated as a perturbation on the free-particle spectrum $E_n = 4E_C n^2$. The nearly free electron model describes electrons in a crystal as weakly interacting with the periodic potential of the atom lattice, which primarily perturbs their behavior by opening energy gaps at the boundaries of the Brillouin zone, while otherwise allowing them to behave similarly to a free electron gas[9]. In the crystal analogy, wavevectors differing by a reciprocal lattice vector are equivalent; here, shifting the momentum origin is equivalent to changing the gate charge n_g. The free-particle parabolas intersect at $n = \pm 1/2$ (the Brillouin-zone

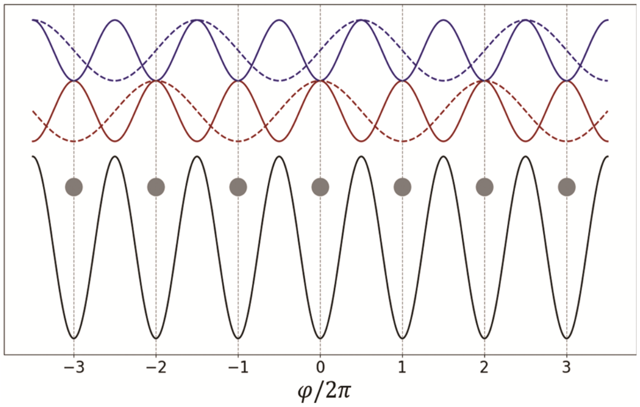

Fig. 2 — On the principle of simulation of one-dimensional crystal lattice. The dotted lines show the even (red) and odd (blue) solutions for the standing wave, and the corresponding solid lines show the probability density for these solutions

boundary), where the unperturbed states $|n = 1/2\rangle$ and $|n = -1/2\rangle$ are degenerate. For a degenerate level (where multiple wavefunctions correspond to the same energy) any linear combination of these wavefunctions also represents a state with that same energy. Consequently, the application of a perturbation not only admixes wavefunctions of states with different energies but also induces a "rotation" of the basis within the degenerate subspace[10]. It is this "rotation" that gives rise to first-order corrections to the energy; their calculation reduces to finding the eigenfunctions of the perturbing operator $U(\varphi)$ within the degenerate subspace. Applying degenerate perturbation theory with $U(\varphi) = -E_J \cos\varphi$ in this two-dimensional subspace, the matrix elements are computed using

$$\cos\hat{\varphi} = \frac{1}{2}\sum_n \left(|n\rangle\langle n+1| + |n+1\rangle\langle n|\right) \qquad \ldots (2)$$

The perturbation matrix is

$$U_{nn'} = \begin{pmatrix} 0 & -E_J/2 \\ -E_J/2 & 0 \end{pmatrix} \qquad \ldots (3)$$

whose eigenvalues $\pm E_J/2$ lift the degeneracy, giving the split energies at $n = 1/2$:

$$E_\pm = E_C \pm \frac{E_J}{2} \qquad \ldots (4)$$

To find the dispersion near the zone boundary, we expand the kinetic term around $n = \pm 1/2$, writing $n = 1/2 + \delta n$. Keeping terms linear in δn, the total Hamiltonian in the subspace becomes

$$H(\delta n) = \begin{pmatrix} 4E_C\delta n & -E_J/2 \\ -E_J/2 & -4E_C\delta n \end{pmatrix} \qquad \ldots (5)$$

Diagonalizing gives

$$E_\pm(\delta n) = E_C \pm \sqrt{\left(\frac{E_J}{2}\right)^2 + (4E_C\delta n)^2} \qquad \ldots (6)$$

showing the characteristic avoided crossing and the opening of a band gap of size E_J at the zone boundary (Fig. 3).

2.2 Strong-Coupling Regime

In the opposite limit ($E_J \gg E_C$), the potential wells are deep, and the low-energy eigenstates are tightly localized near the minima $\varphi = 2\pi p, p \in Z$. This is the strong-coupling limit of the crystal problem, electrons in a crystal remain largely localized around their parent atoms, with their wavefunctions only slightly overlapping with those of neighboring atoms[9]. Tunneling between neighboring deep wells hybridizes the localized states and leads to the formation of energy bands. The band dispersion for the mth level is well approximated by a cosine law[8],

$$E_m(n_g) \approx E_m(n_g = 1/4) - \frac{\epsilon_m}{2}\cos(2\pi n_g) \qquad \ldots (7)$$

where the bandwidth ϵ_m is given by the difference

$$\epsilon_m = E_m(n_g = 1/2) - E_m(n_g = 0) \qquad \ldots (8)$$

For $E_J/E_C \gg 1$, the potential satisfies the quasiclassicality criterion, whereby the de Broglie wavelength λ of a particle varies little on its own scale. In our case, where $\hat{\varphi}$ plays the role of a spatial coordinate, it can be shown that

$$\left|\frac{d\lambda}{d\varphi}\right| \sim \sqrt{\frac{E_C}{E_J}} \ll 1 \qquad \ldots (9)$$

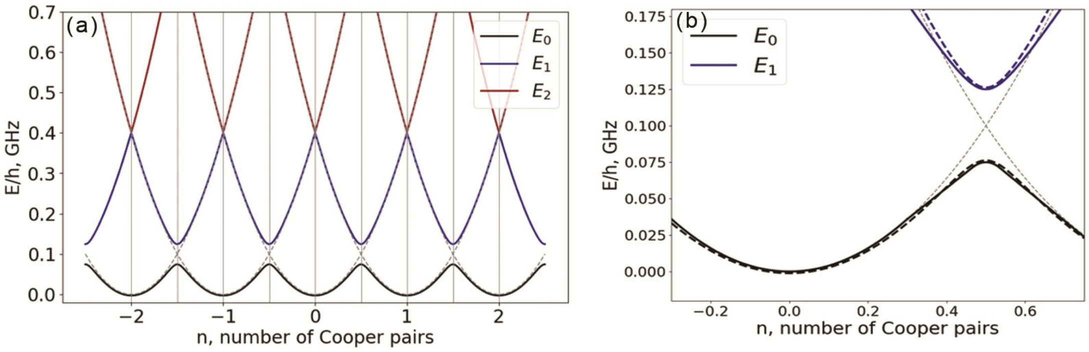

Fig. 3 — Eigenenergies E_m of the qubit Hamiltonian. (a) The first three energy levels calculated by numerical diagonalizing of Hamiltonian; (1). (b) The avoided crossing of the first and the second energy levels calculated analytically using perturbation theory (solid curves) and calculated numerically (dashed curves)

In this regime, the behavior of the system increasingly resembles that of a classical system. This observation highlights intuitive parallel between quantum mechanics and wave optics: as wave optics reduces to geometric optics in the limit of vanishing wavelength, so too does the motion of a quantum particle approach a classical trajectory in the short-wavelength limit. A systematic derivation of the form of the wavefunctions within the Wentzel–Kramers–Brillouin (WKB) approximation proceeds as follows. Starting from the one-dimensional Schrödinger equation, one makes an exponential ansatz $exp(\pm S(\varphi)/\hbar)$ for the wavefunction and subsequently constructs a formal asymptotic expansion for the "action" $S(\varphi)$ in powers of $\hbar$ using an iterative procedure[10]. The WKB (Wentzel–Kramers–Brillouin) quasiclassical method[11,12] yields the asymptotic form of the bandwidth:

$$\epsilon_m \approx (-1)^m E_C \frac{2^{4m+5}}{m!}\sqrt{\frac{2}{\pi}}\left(\frac{E_J}{2E_C}\right)^{\frac{m}{2}+\frac{3}{4}} e^{-\sqrt{8E_J/E_C}} \qquad \ldots (10)$$

Thus, the bands become exponentially narrow as E_J/E_C increases (Fig. 4), reflecting the suppression of tunneling between deep wells. Thus, increase of the ratio E_J/E_C leads to an exponential decrease of the charge dispersion, so qubit transition frequency become extremely stable with respect to charge noise. This is a key advantage of transmon qubits, characterized by high ratio E_J/E_C. This feature allows transmons to be used in quantum processors as computational qubits[13-15] and coupling elements[16,17].

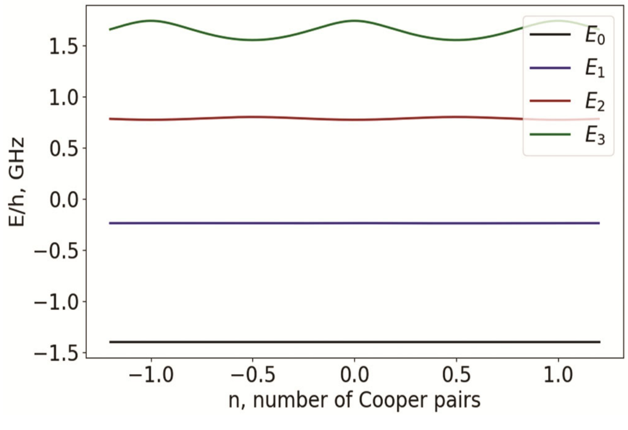

Fig. 4 — Eigenenergies E_m of the qubit Hamiltonian (1) as a function of the charge n in strong-coupling regime ($E_J/E_C = 10$). The first four energy levels calculated by numerical diagonalizing of Hamiltonian (1)

2.3 Tuning the Spectrum with a DC-SQUID

To make the considered quantum simulator more versatile, it is important to be able to switch between different interaction regimes by adjusting the ratio between the Josephson and charging energies. In practice, the Josephson energy E_J is often made tunable by replacing the single junction with a SQUID (Superconducting Quantum Interference Device)[18,19]. Direct current SQUID (DC-SQUID) is a superconducting loop interrupted by two Josephson junctions (Fig. 5). For a SQUID with critical currents I_{ca} and I_{cb}, the total supercurrent is

$$I = I_{ca}\sin\varphi_a + I_{cb}\sin\varphi_b \qquad \ldots (11)$$

where the phase difference across the SQUID, $\varphi = \varphi_b$, and the flux quantization condition gives $\varphi_a = \varphi_b + 2\pi\Phi_{ext}/\Phi_0$. Φ_{ext} is an external magnetic flux, $\Phi_0 = \frac{\pi\hbar}{e}$ is a magnetic flux quantum. The maximum supercurrent (the critical current of the SQUID) is

$$I_{\max} = \sqrt{I_{ca}^2 + I_{cb}^2 + 2I_{ca}I_{cb}\cos\left(2\pi\frac{\Phi_{ext}}{\Phi_0}\right)} \qquad \ldots (12)$$

Introducing $I_{c\Sigma} = I_{ca} + I_{cb}$ and the asymmetry parameter $d = (I_{ca} - I_{cb})/I_{c\Sigma}$, Eq. (12) can be rewritten as

$$I_{\max} = I_{c\Sigma}\cos\left(\frac{\pi\Phi}{\Phi_0}\right)\sqrt{1 + d^2\tan^2\left(\frac{\pi\Phi_{ext}}{\Phi_0}\right)} \qquad \ldots (13)$$

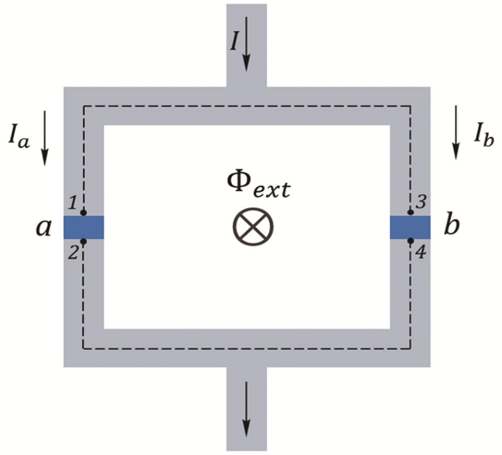

Fig. 5 — Superconducting Quantum Interference Device (SQUID): two parallel connected Josephson junctions a and b (shown in blue). The contour of the SQUID is permeated by an external magnetic flux

Since $E_J = \hbar I_c/(2e)$, the effective Josephson energy of the qubit becomes flux-tunable:

$$E_J(\Phi) = E_{J\Sigma}\left|\cos\left(\frac{\pi\Phi}{\Phi_0}\right)\right|\sqrt{1+d^2\tan^2\left(\frac{\pi\Phi_{ext}}{\Phi_0}\right)}, \qquad E_{J\Sigma} = \frac{\hbar I_{c\Sigma}}{2e} \qquad \dots (14)$$

For a symmetric SQUID ($I_{ca} = I_{cb}, d = 0$), the formula for the effective Josephson energy is simplified:

$$E_J(\Phi) = E_{J\Sigma}\left|\cos\left(\frac{\pi\Phi_{ext}}{\Phi_0}\right)\right| \qquad \dots (14)$$

By varying the magnetic flux Φ_{ext}, one can therefore continuously sweep the system from the weak-coupling ($E_J \ll E_C$) to the strong-coupling ($E_J \gg E_C$) regime, covering all intermediate cases. The symmetric DC-SQUID described by formula (15) can tune the Josephson energy to arbitrarily small values. Thus, by choosing a relatively small charging energy ($E_C/h \approx 0.1$ GHz) and using a DC-SQUID with identical Josephson junctions ($E_{Ja}/h = E_{Jb}/h \approx 1$ GHz), the ratio $E_J(\Phi)/E_C$ can be varied over a wide range, switching the simulator between the weak- and strong-coupling regimes. The proposed energy parameters are technologically feasible and operational in experiments[20]. The Josephson energy is determined by the critical current I_c of the junction according to the formula $E_J = \hbar I_c/(2e)$. A Josephson energy of 1 GHz corresponds to a critical current of approximately 2 nA. There exists established fabrication experience for producing Josephson junctions with such parameters[21].

2.4 Experimental Concept: Two-Tone Spectroscopy

To experimentally observe the band structure described theoretically in the previous sections, a method is required to measure the qubit transition frequency as a continuous function of the external flux Φ, which controls the effective lattice depth $E_J(\Phi)$. The qubit's flux-dependent transition spectrum can be mapped experimentally using two-tone spectroscopy. Various techniques exist for readout the quantum state of a qubit, including resonant readout using a SQUID[22], readout via a quantum point contact[23,24], and the most widely adopted method — dispersive readout employing a resonator coupled to the qubit[19]. The dispersive readout approach underlies the two-tone spectroscopy concept. Figure 6 shows the equivalent circuit of the qubit capacitively coupled to the resonator. The measurement scheme involves two independent microwave drives. The first one is a probe tone of fixed frequency ω_p applied to the readout resonator to monitor its response. The second tone is a pump tone of variable frequency ω_d applied directly to the qubit to excite transitions. The system Hamiltonian in the presence of these drives is

$$\hat H(t) = \hat H_0 + \hat H_{\text{drive}}(t) \qquad \dots (16)$$

where the unperturbed part is

$$\hat H_0 = \frac{\hbar\omega_q}{2}\hat\sigma_z + \hbar\omega_r \hat a^\dagger \hat a + \hbar g\left(\hat a + \hat a^\dagger\right)\hat\sigma_x \qquad \dots (17)$$

and the drive term explicitly contains both signals:

$$\hat H_{\text{drive}}(t) = \hbar\epsilon_p\left(\hat a + \hat a^\dagger\right)\cos\left(\omega_p t\right) + \hbar\epsilon_d\hat\sigma_x\cos(\omega_d t) \qquad \dots (18)$$

Here ϵ_p and ϵ_d are the amplitudes of the probe and pump drives, respectively. The detection relies on the input-output formalism for the resonator. The Heisenberg equation for the resonator mode $\hat a(t)$, including coupling to a transmission line with decay rate κ, is

$$\dot{\hat a} = -i\left[\hat a, \hat H_0\right] - \frac{\kappa}{2}\hat a - i\epsilon_p e^{-i\omega_p t} - \sqrt{\kappa}\,\hat b_{\text{in}}(t) \qquad \dots (19)$$

where $\hat b_{\text{in}}(t)$ is the quantum operator representing the incoming field on the transmission line. The considered resonator dissipation model is not applicable in the case of strong coupling[25]. The input-output relation

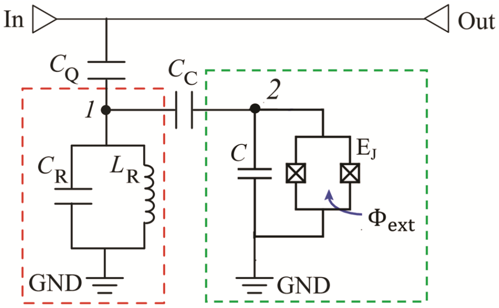

Fig. 6 — Equivalent circuit of the qubit capacitively coupled to the resonator

$$\hat{b}_{\text{out}}(t) = \hat{b}_{\text{in}}(t) + \sqrt{\kappa}\,\hat{a}(t) \qquad \dots (20)$$

connects the outgoing field $\hat{b}_{\text{out}}$ to the intra-resonator field. In the dispersive regime ($|\Delta| = |\omega_q - \omega_r| \gg g$), the effective Hamiltonian obtained via a Schrieffer-Wolff transformation[26] is

$$\hat{H}_{\text{disp}} \approx \frac{\hbar}{2}\left(\omega_q + 2\chi\hat{a}^{\dagger}\hat{a}\right)\hat{\sigma}_z + \hbar(\omega_r + \chi\hat{\sigma}_z)\hat{a}^{\dagger}\hat{a} \qquad \dots (21)$$

with $\chi = g^2/\Delta$. The resonator frequency is shifted by $\pm\chi$ depending on the qubit state ($\langle\hat{\sigma}_z\rangle = \pm 1$).

For a weak probe, the steady-state resonator response can be treated linearly. The expectation value $\alpha = \langle\hat{a}\rangle$ satisfies

$$\dot{\alpha} = -\left[i(\omega_r + \chi\langle\hat{\sigma}_z\rangle) + \frac{\kappa}{2}\right]\alpha - i\epsilon_p e^{-i\omega_p t} \qquad \dots (22)$$

In the rotating frame at ω_p, the stationary solution is

$$\alpha = \frac{-i\epsilon_p}{i[\omega_p - \omega_r - \chi\langle\hat{\sigma}_z\rangle] + \kappa/2} \qquad \dots (23)$$

Substituting into the input-output relation and taking the average gives the complex transmission coefficient

$$S_{21}(\omega_p) = \frac{\langle\hat{b}_{\text{out}}\rangle}{\langle\hat{b}_{\text{in}}\rangle} = 1 - \frac{\kappa}{i[\omega_p - \omega_r - \chi\langle\hat{\sigma}_z\rangle] + \kappa/2} \qquad \dots (24)$$

The qubit state population $\langle\hat{\sigma}_z\rangle$ is controlled by the pump tone. When ω_d matches the qubit transition frequency $\omega_q' = \omega_q + 2\chi\langle\hat{a}^{\dagger}\hat{a}\rangle$, the qubit is excited, changing $\langle\hat{\sigma}_z\rangle$ from -1 (ground) towards 1 (excited). This shifts the effective resonator frequency $\omega_r \to \omega_r + \chi\langle\hat{\sigma}_z\rangle$, altering S_{21}. Thus, by fixing ω_p near ω_r and sweeping ω_d and the flux Φ (which tunes ω_q), one records dips in $|S_{21}|$ or shifts in its phase whenever ω_d crosses a qubit transition. This produces a two-dimensional map $S_{21}(\omega_d, \Phi)$ that directly visualizes the qubit's flux-dependent spectrum.

2.5 Numerical Calculation Details

The energy spectrum of the qubit was obtained by numerical diagonalization of its Hamiltonian in the charge basis. The operator for the number of Cooper pairs $\hat{n}$, was discretized on a finite symmetric grid. In the numerical simulation the first six eigenstates were taken into account. The Hamiltonian matrix was constructed using a second-order finite-difference scheme, with zero boundary conditions imposed on the wave function at the grid boundaries. The resulting large, sparse, Hermitian matrix was diagonalized using the implicitly restarted Lanczos method[27]. This approach is well-suited for sparse Hermitian eigenvalue problems. The calculation targeted the smallest algebraic eigenvalues, and a high iteration limit of 4000 was set to achieve robust numerical convergence. The convergence of the numerical method is confirmed by comparing its results with approximate analytical models (perturbation theory and quasi-classical approximation) for parameter regimes where their respective strong- and weak-coupling approximations are valid. The discrepancy between the results obtained using analytical and numerical methods does not exceed 1 %.

A numerical simulation of the two-tone spectroscopy process was performed by solving the time-dependent Schrödinger equation for the composite Hamiltonian of the qubit and resonator with two pump signals applied to the resonator (the first tone) and the qubit (the second tone). Scanning was performed over the frequency of the signal applied to the qubit and over the magnitude of the magnetic flux in the qubit loop. The qubit and resonator are represented as two-level systems, which limits the correct description of the process only to the case of a small number of photons in the resonator and a low probability of populating the second excited state of the qubit. To simulate the dependence of the S_{21} parameter on signal frequency and magnetic flux, the phenomenological formula (24) for the linear response of the resonator was used, relating the reflection coefficient to the shift in the effective resonator frequency, which depends on the qubit state. The numerical solution of the time-dependent Schrodinger equation was performed by the adaptive Runge-Kutta method of order 5(4). This method uses the Dormand-Prince pair of formulas[28], the error is controlled assuming accuracy of the fourth-order method accuracy, but steps are taken using the fifth-order accurate formula. To ensure the high fidelity required for quantum dynamical simulations, the relative error tolerance was set to 10^{-8}. This strict criterion guarantees the convergence of the numerical solution by forcing the adaptive step-size controller to maintain the local truncation error per step at an extremely small fraction of the solution's magnitude. It is essential for accurately resolving the rapid oscillatory phases inherent in quantum evolution of the considered “qubit-resonator” system, preserving the unitary norm of the wavefunction, and ensuring the reliability of subsequent physical observables. Maximum time step, which was set to 10^{-11} s, provides an upper bound to explicitly capture the fastest dynamics present in the system, forming a robust convergence. The preservation of the normalization of the wave function of the full “qubit-resonator” system was verified, with the numerical error not exceeding 10^{-5}.

3 Results and Discussion

Numerical simulation was performed for the circuit parameters shown in Table 1. Figure 7 (a) shows a numerically calculated two-dimensional map of the phase of the S_{21} parameter versus the frequency of the second tone and the external magnetic flux. In the calculation, the qubit was assumed to have a charging energy of $E_C/h = 0.1$ GHz, the Josephson energies of the symmetric SQUID junctions were $E_{Ja}/h = E_{Jb}/h = 1$ GHz, and the resonator had a frequency of 7 GHz with a quality factor of 4000. The plot indicates two characteristic points: point "1" at zero external flux, corresponding to the maximum Josephson energy ($E_J(\Phi = 0)/E_C = 20$), and point "2" at half a flux quantum, where the Josephson energy become zero according to Eq. (15). Thus, at point "1", the strong-coupling regime is realized (Fig. 7 (b)), while at point "2", the energy gaps in the charge dispersion disappear — the extreme case of the weak-coupling regime (Fig. 7 (c)). The experimentally obtained spectrum (Fig. 7 (a)) can be interpreted as the dependence of the transition energy between adjacent bands is the center of the Brillouin zone (at the Γ-point) on the depth of the periodic potential.

The potential impact of realistic device imperfections on the operation of the proposed quantum simulator is considered. The most critical parameter characterizing the imperfection of the proposed two-tone spectroscopy setup is the quality factor of the resonator. The amplitude–frequency response of the readout circuit, which comprises the resonator and the output line, is governed by two quantities: the external quality factor Q, associated with energy loss into the matched readout line and measurement apparatus, and the internal quality factor

Table 1 — Device parameters that used in the numerical calculation

Charge energy E_C, GHz	Josephson energies of SQUID junctions E_{Ja}, E_{Jb}, GHz	Critical current of SQUID junctions I_a, I_b, nA	Resonator frequency $\omega_r/2\pi$, GHz	Dispersive shift χ, MHz	Quality factor of resonator
0.1	1	2	7	10	4000

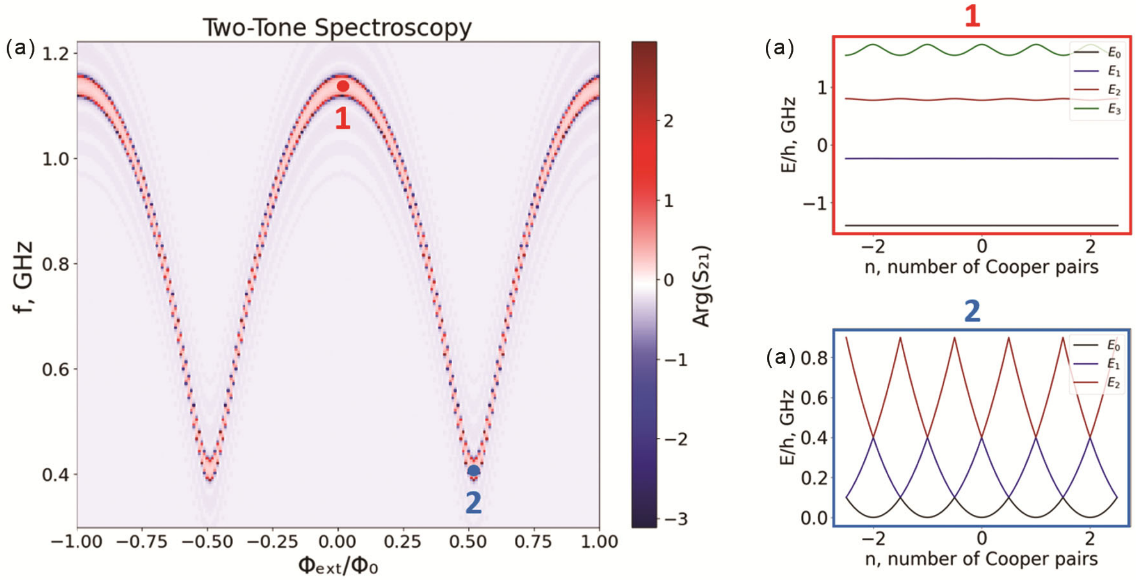

Fig. 7 — (a) Map of the phase of the S_{21} parameter versus the frequency of the second tone and the magnetic flux. (b) The strong-coupling regime at point 1 (zero external flux). (c) The extreme case of the weak-coupling regime at point 2 (half a flux quantum)

Q_{int}, associated with losses intrinsic to the resonator (electrically modeled as a series resistor in the LC circuit). As established in prior experimental studies[29,30] the internal quality factor of the readout resonator typically exceeds its external counterpart by an order of magnitude. Consequently, in the theoretical analysis presented in only the external quality factor, which determines the decay rate into the readout line has been taken into account. As shown by formula (24), this parameter directly determines the width of the Lorentzian peak in the spectroscopic response. Coherent characteristics of superconducting qubits (relaxation time and dephasing time) are key parameters that determine the feasibility of noise-resilient quantum computing. However, in the experimental scheme described in the paper, these coherent characteristics of a qubit are not critical limiting factors. This is because the proposed quantum simulation relies on spectroscopic measurement of a qubit under continuous microwave pump. This distinction highlights a fundamental difference between analog quantum simulators and universal quantum processors: the latter rely on sequences of time-limited control pulses and require qubits to retain their quantum states with high fidelity throughout algorithm execution. In contrast, experiments involving spectroscopy of a qubit–resonator system impose no such requirement. Indeed, several studies[31,32] have successfully resolved spectral features of such systems with qubit relaxation and dephasing times on the order of several microseconds – values nearly two orders of magnitude lower than those routinely achieved with state-of-the-art quantum device technologies. This robustness is particularly relevant in the context of the present experiment, where the magnetic flux through the qubit loop is tuned away from the so-called "sweet spots" – operating points at which the qubit transition frequency is first-order insensitive to flux noise. There are two "sweet spots": first one corresponds to the zero magnetic flux in the qubit loop (point 1 on Fig. 7 (a)), second one corresponds to the flux degenerate point $\Phi_0/2$ (point 2 on Fig. 7 (a)). At other flux bias values, the qubit becomes susceptible to flux noise, resulting in a reduction of the dephasing time. In addition, the measured full band structure of the simulated one-dimensional crystal includes transitions between highly excited states of the qubit, which exhibit significantly shorter relaxation and coherence times[33]. Imperfections in the fabrication of Josephson junctions can lead to asymmetry in the SQUID. As a result, a small nonzero asymmetry parameter d may arise, causing the effective Josephson energy to remain finite at an external flux equal to half a magnetic flux quantum, taking a value of $E_{J\Sigma}|d|$, according to formula (12). This imposes a limitation on the minimum achievable depth of the periodic potential in the weak-coupling regime.

4 Conclusion

A simple yet powerful quantum simulation platform based on a superconducting qubit is proposed and theoretically analyzed. The system naturally reproduces the band structure physics of a one-dimensional crystal, with the phase across the Josephson junction acting as a spatial coordinate and the charge acting as a quasimomentum. By tuning the ratio E_J/E_C via an external magnetic flux applied to a DC-SQUID, the simulator can access both the nearly-free electron and tight-binding regimes, as well as all intermediate cases. In the weak-coupling limit, a band gap opens at the Brillouin zone boundary due to degenerate perturbation theory. In the strong-coupling limit, bands become exponentially narrow, reflecting suppressed tunneling between deep potential wells a regime directly relevant to the charge noise insensitivity of transmon qubits. The two-tone spectroscopy technique provides a direct experimental method to map the flux-dependent energy spectrum, visualizing the simulator's energy transitions. This work bridges the fields of superconducting quantum circuits and condensed matter physics, highlighting the potential of artificial quantum systems as programmable simulators for exploring fundamental models. The proposed device is technologically feasible with current superconducting qubit architectures and opens a pathway for simulating more complex quantum many-body phenomena in engineered lattices.

References

1 DiCarlo L, Chow J, Gambetta J, *et al.*, *Nature,* 460 (2009) 240.

2 Kjaergaard M, Schwartz M E, Braumüller J, *et al.*, *Annu Rev Condens Matter Phys*, 11 (2020) 369.

3 Kumar T, Kumar D & Singh G, *Indian J Pure Appl Phys*, 61 (2023) 355.

4 Greenaway S, Smith A, Mintert F & Malz D, Quantum, 8 (2024) 1263.

5 Orell T, Michailidis A A, Serbyn M & Silveri M, *Phys Rev B*, 100 (2019) 134504.

6 Mansikkamaki O, Laine S, Piltonen A & Silveri M, *PRX Quantum*, 3 (2022) 040314.

7 Gu X, Kockum A F, Miranowicz A, Liu Y & Nori F, *Phys Report*, 718 (2017) 1.
8 Koch J, Yu T M, Gambetta J, *et al.*, *Phys Rev A*, 76 (2007) 042319.
9 Abrikosov A A, Fundamentals of the theory of metals (North-Holland, Amsterdam), 1988 p. 296.
10 Landau L D & Lifshitz E M, Quantum Mechanics (Pergamon, New York), 1977 p. 133.
11 Goldstein S, *Proc R Soc Edinburgh*, 49 (1929) 210.
12 Connor J N L, Uzer T, Marcus R A & Smith A D, *J Chem Phys*, 80 (1984) 5095.
13 Arute F, Arya K, Babbush R, *et al.*, *Nature*, 574 (2019) 505.
14 O'Malley P J J, Babbush R, Kivlichan I D, *et al.*, *Phys Rev X*, 6 (2016) 031007.
15 Sun S, Marinelli B, Koh J M, *et al.*, *npj Quant Inform*, 10 (2024) 55.
16 Ding L, Hays M, Sung M, *et al.*, *Phys Rev X*, 13 (2023) 031035.
17 Berezkin N G, Simakov I A & Mazhorin G S, *Tech Phys Lett*, 51 (2025) 107.
18 Shramkova O V, Lazarides N, Tsironis G P & Ustinov A V, *Appl Phys A*, 123 (2017) 58.
19 Krantz P, Kjaergaard M, Yan F, *et al.*, *Appl Phys Rev*, 6 (2019) 021318.
20 Barends R, Kelly J, Megrant A, *et al.*, *Phys Rev Lett*, 111 (2013) 080502.
21 Peruzzo M, Hassani F, Szep G, *et al.*, *PRX Quantum*, 2 (2021) 040341.
22 Lee J C, Oliver W D, Orlando T P & Berggren K K, *IEEE Trans Appl Supercond*, 15 (2005) 841.
23 Elzerman J, Hanson R, van Beveren W L, *et al.*, *Nature*, 430 (2004) 431.
24 Berezkin N G, *Bullet Perm Univer Phys*, 67 (2025) 21.
25 Beaudoin F, Gambetta J M & Blais A, *Phys Rev A*, 84 (2011) 043832.
26 Bravyi S, DiVincenzo D & Loss D, *Annals Phys*, 326 (2011) 2793.
27 Lanczos C, *J Res Natl Bur Stand,* 45 (1950) 255.
28 Dormand J R & Prince P J, *J Comput Appl Math*, 6 (1980) 19.
29 Manucharyan V E, Masluk N A, Kamal A, *et al.*, *Phys Rev B*, 85 (2012) 024521.
30 Nigro A, Jutzi E, Oppliger F, *et. al.*, *ACS Appl Electron Mater*, 6 (2024) 5094.
31 Suri B, Keane Z K, Ruskov R, *et. al.*, *New J Phys*, 15 (2013) 125007.
32 Fedorov G P, Yursa V B, Efimov A E, *et. al.*, *Phys Rev A*, 102 (2020) 013707.
33 Peterer M J, Bader S J, Jin X, *et al.*, *Phys Rev Lett*, 114 (2015) 010501.